frontiers in Energy Research

ORIGINAL RESEARCH
published: 24 January 2020
doi: 10.3389/fenrg.2019.00157

Ferroconcrete-Like Helical Carbon Nanotube/Reduced Graphene Oxide Heterostructure 3D Networks as Sulfur Hosts for High-Performance Li-S Batteries

Zhangbin Luo†, Zengren Tao†, Xinyu Li, Dandan Xu, Congxu Xuan, Zhun Wang, Tao Tang, Jianfeng Wen*, Ming Li and Jianrong Xiao**

Ministry-Province Jointly-Constructed Cultivation Base for State Key Laboratory of Processing for Non-Ferrous Metal and Featured Materials & Key Laboratory of Nonferrous Materials and New Processing Technology, College of Science, Guilin University of Technology, Guilin, China

OPEN ACCESS

Edited by:
Teng Zhai,
Nanjing University of Science and Technology, China

Reviewed by:
Tianyu Liu,
Virginia Tech, United States
Xifei Li,
Xi'an University of Technology, China
Qiubo Guo,
Nanjing University of Science and Technology, China

***Correspondence:**
Xinyu Li
lixinyu5260@163.com
Jianfeng Wen
wjfculater@163.com
Jianrong Xiao
xjr@glut.edu.cn

†These authors have contributed equally to this work

Specialty section:
This article was submitted to Electrochemical Energy Conversion and Storage, a section of the journal Frontiers in Energy Research

Received: *24 October 2019*
Accepted: *09 December 2019*
Published: *24 January 2020*

Citation:
Luo Z, Tao Z, Li X, Xu D, Xuan C, Wang Z, Tang T, Wen J, Li M and Xiao J (2020) Ferroconcrete-Like Helical Carbon Nanotube/Reduced Graphene Oxide Heterostructure 3D Networks as Sulfur Hosts for High-Performance Li-S Batteries. Front. Energy Res. 7:157. doi: 10.3389/fenrg.2019.00157

A novel helical Carbon nanotubes (HCNT) network with a reduced graphene oxide (rGO) coating was designed and fabricated through a synergistic self-assembly and sulfuration strategy for use as an effective sulfur (S) host. A ferroconcrete frame structure with a hierarchical 3D nanostructure composed of 1D HCNT and 2D rGO nanosheets was obtained. The rGO wraps around the HCNT to form a heterostructure and provide an apparent coating that protects S. HCNT in the composite is boosted to create a 3D network architecture and reinforce the structural stability. Moreover, the heterostructures and rGO coatings, which are rich in wrinkles, can greatly minimize direct contact between the polysulfide and electrolyte; they also provide an abundance of active sites and boundary defects. Furthermore, the 3D interconnected structure creates effective ion diffusion channels and allows effective trapping of S and Li polysulfides. When used as a cathode, the HCNT/rGO/S cathode exhibits a high initial specific capacity of 1,196 mAh g^{-1} at 0.1 C. The capacity decay rate of the HCNT/rGO/S is only 0.075% per cycle after cycling for 200 times at a rate of 0.1 C. This unique hybrid HCNT/rGO/S electrode design may motivate the development of other high-performance electrodes with excellent electrochemical properties.

Keywords: helical carbon nanotube, reduced graphene oxide, heterostructure, 3D hybrid materials, lithium–sulfur batteries

INTRODUCTION

Under the situation of new energy, electric vehicles based on Li-ion power batteries are widely considered a development thrust for next-generation automobiles (Kim et al., 2013; Manthiram et al., 2013; Song et al., 2013). Li-ion batteries, which commonly use $LiCoO_2$ or $LiFePO_4$ as a cathode material, are limited by their low practical energy density. Thus, intensive studies have been conducted to develop rechargeable batteries with high energy density, good cycle performance, and low cost to meet the market demand for energy storage. Among the numerous battery systems currently available, Li-S batteries (LSBs) were proposed as a promising candidate for power batteries and have attracted considerable attention. LSBs have high theoretical specific capacity

(1,675 mAh g^{-1}); their energy density (2,600 Wh kg^{-1}) is 2–3 times of current Li-ion batteries, are inexpensive, and employ low-toxicity active materials. Despite the recent great progress in LSBs, however, the applications of these batteries are restrained by several critical challenges (Liu et al., 2017; Gu et al., 2018; Xiaofei et al., 2018). These problems mainly originate from volume expansion, the extremely low conductivity of S, and the shuttle effect and limit the electrochemical stability and coulombic efficiency of the cell during cycling and resting.

Numerous strategies, such as novel nanostructured S cathodes (Wang C. et al., 2014), modification of the electrolyte adjustment separator (Yan et al., 2013; Wang et al., 2015), and protected Li metal anodes (Zhang H. et al., 2018), have been proposed to enhance the LSBs' electrochemical performance. Various C structures, such as C nanotubes (CNTs) and graphene oxide (GO), have been developed as highly promising hosts for S cathodes (Hu et al., 2017; Tan et al., 2018). In particular, GO is highly suitable for coating the surface of C–S nanocomposites to form a cladding structure because the unique 2D structure and excellent physicochemical properties of GO improve the cycle performance of LSBs (Kim et al., 2012). CNTs present unique nanostructures with excellent electrical conductivity and can form heterostructure in three dimensions (Gulzar et al., 2018). However, both forms of CNT and GO easily aggregate due to strong van der Waals interactions, thereby degrading the effective specific surface area (SSA) and available space. Thus, it is essential to design composite carbon materials that integrate CNTs and GO with 3D structural carbon matrix as host materials for sulfur cathodes. And these hybrid cathodes with CNTs and GO exhibit enhanced electrochemical performance on account of their synergistic effect (Ding et al., 2016; Wang et al., 2016; Yang et al., 2018). Heterostructures can be formed by synthesizing mixed 1D CNTs and 2D GO, and these structures can be assembled into 3D superstructures. The constructed heterostructures can not only hasten the transport kinetics in the crystal structures but also preserve the nanocrystal structures. The construction of heterostructures has immense potential in improving energy conversion and storage properties (Sun et al., 2011; Zhang et al., 2019).

Modification of S cathodes with graphene and CNTs is still in its initial stages, and more structural designs are needed to obtain S cathodes with improved electrochemical performance. Chiral C-based nanotubes with helical structures (HCNT), large specific surface areas, and numerous surface grooves are highly desired in LSBs because of their outstanding electrochemical performance, extraordinary self-weaving behavior, and light weight. HCNTs are used to construct interwoven conductive networks for the rapid transfer of electrons, and the 3D mesh structure formed provides attachment sites for S (Akagi et al., 1995; Tang et al., 2010; Li et al., 2018). These characteristics inhibit the dissolution and diffusion of polysulfides and adapt to the volume expansion effect in the discharge process. Thus, these characteristics improve the cycling life of the S cathode (Jin et al., 2016). In addition, compared with straight CNTs, HCNT can be more easily twisted, bent, and stretched (Di et al., 2016). HCNT can also have a nested structure because graphene stacks up to form multilayer structures. The rational design and fabrication of graphene films with optimized 3D architectures are an effective approach to avoid the restacking of graphene and shorten ion-diffusion paths. These films possess a large surface area, porous structures, and excellent electrical conductivity. Moreover, the films can be easily formed by introducing HCNTs to the GO framework. Thus, the electrochemical performance is enhanced (Peng et al., 2014; Su et al., 2017). Twisted CNT yarns, for example, have been developed to harvest electrical energy. Kar (Cherusseri et al., 2016) prepared hierarchical HCNT/C fiber structure electrodes for use as flexible supercapacitors and obtained a maximum gravimetric capacitance of 125.7 F g^{-1} at a current density of 0.28 mA cm^{-2}. Although helical structures have been well-studied for converting tensile or torsional mechanical energy into electrical energy, the use of HCNT and GO in LSBs has rarely been reported.

In this work, we designed and fabricated a cathode composed of a rGO-coated HCNT heterostructure composite with a 3D ferroconcrete-like structure as a S container (HCNT/rGO/S) through a facile and scalable solution-based self-assembly method. Here, the HCNTs and rGO serve as the ferroconcrete-like frame structure, and rGO provides an external coating that protects S and forms a heterostructure. The S particles are well-coated and confined to the 3D ferroconcrete-like nanostructures. The HCNTs prompt the formation of an interconnected 3D network architecture with highly robust conductive networks that can boost electron transport and maintain structural integrity. The rGO coatings with abundant wrinkles and voids can greatly increase both surface area and interfaces contact, which are beneficial for accommodating volume expansion and minimize direct contact between the polysulfide with the electrolyte. The unique 1D/2D HCNT/rGO heterostructure provides abundant active sites and boundary defects while ameliorating the nucleation/conversion redox kinetics and decreasing the overpotential of polysulfide nucleation. When used as a cathode, a battery made of the proposed HCNT/rGO/S heterostructure can achieve high initial specific capacities of 1,196, 1,130, and 1,009 mAh g^{-1} at 0.1, 0.2, and 0.5 C, respectively. Furthermore, the HCNT/rGO/S cathode provides a high specific capacity of 1,016, 971.8, and 872 mAh g^{-1} at 0.1, 0.2, and 0.5 C, respectively, after 200 cycles. These results suggest that the fabricated cathode is a promising candidate for ultrafast charge/discharge applications.

EXPERIMENTAL SECTION

Preparation of Helical Carbon Nanotubes and the 1D/2D Helical Carbon Nanotube/Graphene Oxide Heterostructure

Pristine HCNTs were synthesized via catalytic CVD as reported previously (Tang et al., 2010). The catalyst precursor was prepared from citric acid and $Ni(NO_3)_2$. The CVD method used the catalyst precursor as a raw material to change the temperature and gas flow rate to control the material morphology. In order to enhance chemical compatibility with a suitable solvent, we performed a typical mixed acid (H_2SO_4 and HNO_3 in a 3:1 ratio) and produced a hydrophilic O group on the surface of

the HCNT. GO was prepared via a modified Hummers' method (Xu et al., 2017). 0.1 g GO powder and 0.1 g acid-treated HCNTs were separately dispersed into the 100 ml N-Methyl pyrrolidone (NMP) and sonicated for 2 h. Then, the GO dispersions and HCNT dispersions were mixed together at a volume ratio of 3:1 and ultrasonicated for 1 h to prepare a mixture of HCNT/GO. During the ultrasound process, the temperature is maintained within 50°C.

Preparation of the Helical Carbon Nanotubes/Reduced Graphene Oxide/Sulfur, Helical Carbon Nanotube/Sulfur, and Reduced Graphene Oxide/Sulfur Active Material

In a typical synthesis procedure, 6.9 g $Na_2S_2O_3$ was first dissolved into the 100 ml HCNT/GO NMP dispersion, ultrasonicated, and then magnetically stirred. Thereafter, 2.7 g concentrated HCl was diluted into an aqueous solution of 0.1 mol l^{-1}, and added dropwise to the above solution at a rate of 10 ml min^{-1} and stirred for 10 min. HCl (0.1 M) was added dropwise into the above well-mixed solution under strong magnetic stirring to obtain an HCNT/GO-S solution and sonicated for 2 h at 90°C to obtain an HCNT/rGO/S solution. Simultaneous sulfuration of GO and elimination of the O-containing functional groups on the GO rendered the formation of the HCNT/rGO/S hybrid material. Finally, the HCNT/rGO/S composite was obtained by centrifugation and drying. HCNT/S and rGO/S were synthesized via the same procedures applied to obtain the HCNT/rGO/S.

Fabrication of the Helical Carbon Nanotubes/Reduced Graphene Oxide/Sulfur, Helical Carbon Nanotubes/Sulfur, and Reduced Graphene Oxide/Sulfur Cathodes

For preparing HCNT/rGO/S working electrodes, a mixture of HCNT/rGO/S composite, Super P, and poly-(vinyl difluoride) (PVDF) binder in the NMP at a mass ratio of 80:10:10 was pasted on an Al foil. The cathode slurry was spread onto Al foil with a doctor blade and then dried for 12 h at 60°C under vacuum. Finally, the cathode was punched into disks with a diameter of 16 mm with an active-material loading of about 1 mg cm^{-2} for assembly, and the HCNT/rGO/S cathode was obtained. HCNT/S and rGO/S were synthesized via the same procedures applied to obtain the HCNT/rGO/S.

Electrochemical Characterization

CR-2025 button cell was used to test the electrochemical properties of the S cathode, and the cell was assembled in the glove box filled with Ar. A Li sheet was used as the anode electrode. The working cathodes and Li anodes were connected to an Al foil and Ni foil, respectively. Celgard 2400 was used to separate the cathodes and anodes. The electrolyte contained a mixture of 1,3-dioxolane and 1,2-dimethoxyethane with 1 M bis sulfonamide Li salt and $LiNO_3$ (1 wt%) dissolved into it. The electrolyte volume for each cell was ∼50 μl. Before electrochemical measurements, the assembled coin-type cells were kept at 25°C for 30 min. A CHI750E electrochemical measurement system was used for cyclic voltammetry (CV) and electrochemical impedance spectroscopy (EIS) measurements. CV was conducted at a scan rate of 0.1 mV s^{-1} in the potential window from 1.5 to 3.0 V. EIS spectra were recorded over frequencies ranging from 0.01 Hz to 100 kHz. The cells were charged/discharged in the potential range from 1.5 to 2.8 V. The specific capacity values were calculated based on the mass of sulfur in the cathode. All experiments were carried out and analyzed at room temperature.

Materials Characterization

The crystal structure and state of the samples were detected by X-ray diffraction (XRD) with Cu Kα radiation in the range of 5–65°. The topographical characteristics of the sample were determined by scanning electron microscopy (SEM) and Transmission electron microscope (TEM). Elemental analysis and distributions were characterized by energy dispersive spectroscopy (EDS), and the crystalline structures of the samples were determined by Raman spectra. X-ray photoelectron spectroscopy (XPS) was conducted to survey the chemical states of the composites. The mass of active material in the electrode was characterized by thermogravimetric analysis (TGA).

RESULTS AND DISCUSSION

Configuration and Morphology

The preparation of HCNT/rGO/S composite with 3D ferroconcrete-like heterostructure is shown in **Figure 1a**. Briefly, GO was prepared via a modified Hummers' method. HCNTs were synthesized by CVD as reported previously (Tang et al., 2010; Xu et al., 2017). In order to enhance the chemical compatibility between components, we treated the HCNTs with a typical mixed acid (H_2SO_4 and HNO_3 at a volume ratio of 3:1), and hydrophilic O groups were produced on the surface of the HCNTs. The HCNTs were first loaded onto the GO by simple bath sonication to increase the conductivity of the GO sheets and the final composite material. Thereafter, π-π bonds were created via H bonding on the carboxyl groups on the GO and acid-treated HCNT surfaces. This step facilitates tight bonding of the two materials (Yu et al., 2014). Then, the HCNTs and GO were dispersed in NMP to form a homogeneous mixture via vigorous ultrasonication treatment. Because the GO sheets contained hydrophobic aromatic regions that could interact with HCNT and highly hydrophilic regions for dispersion in water, therefore the HCNTs and GO were dispersed in NMP to form a homogeneous mixture via vigorous ultrasonication treatment. Given intrinsic van der Waals forces among the HCNT and GO components, the scaffolds supported the porous C nanosheets, and the 2D structures were transformed into 3D interconnected hierarchical porous structures. To synthesize the S particles, $Na_2S_2O_3$ was dissolved in the HCNT/GO dispersions, and HCl was added to this mixture. After ultrasonic hydrothermal reduction, the S nanoparticles attached to the GO sheet were wrapped by the shrunken rGO sheets, and the HCNTs formed electron channels between the inclusions. In

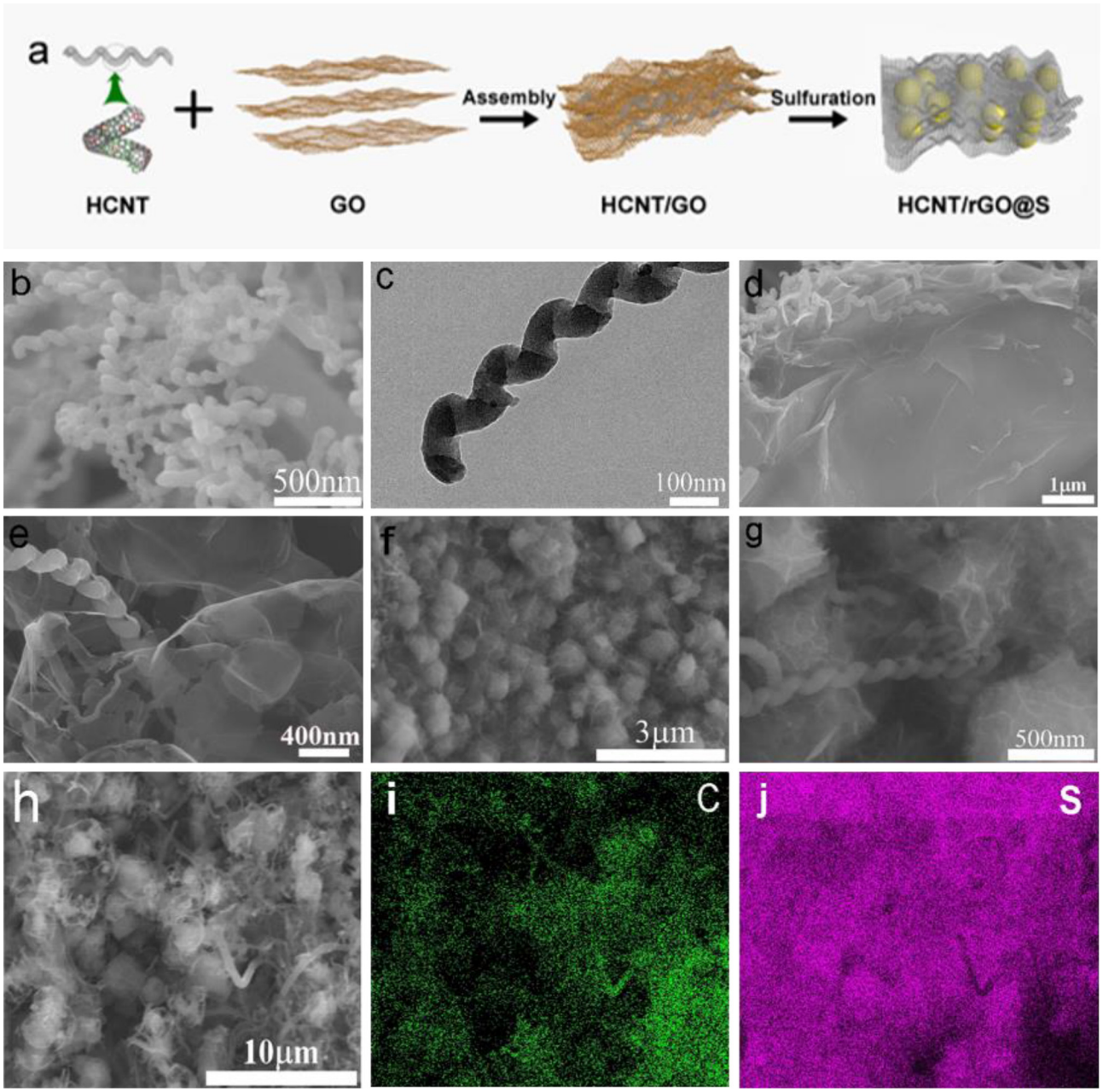

FIGURE 1 | (a) Schematic of the synthetic process of the helical carbon nanotubes (HCNT)/reduced graphene oxide (rGO)/sulfur (S) electrode. The SEM **(b)** and Transmission electron microscope (TEM) **(c)** image of HCNTs. The SEM **(d,e)** of HCNT/GO. The SEM **(f,g)** of HCNT/rGO/S. **(h)** SEM images and **(i,j)** elemental mapping of the HCNT/rGO/S cathode.

our approach, a mildly oxidized HCNT/GO material was used to form composites with the S particles. The GO surfactant was used as a capping agent for the S particles and limited the size of these particles to the submicrometer region during synthesis. Small S particle sizes favor the high specific capacity and rate capability of the S cathodes. The HCNT/GO suspension was mixed with S particles to afford the final S–GO composite. S, which was mainly encapsulated into the abundant hierarchical pores of rGO and HCNT, clearly provides a highly robust conductive pathway for electron transport. The HCNT and rGO were weaved into porous framework, forming a self-obtained 3D interconnected HCNT/rGO.

The morphology and microstructure of the HCNT, HCNT/GO, and HCNT/rGO/S were investigated by SEM. **Figure 1b** shows a SEM image of the pristine HCNTs, in which most of the samples have spiral structures. Sufficient void spaces

and micron-sized spatial dimensions of HCNT with an average length of 5–8 μm are generated by the randomly interconnected HCNTs, which can hold a large amount of active material. This process maintains high electrolyte absorbability and effectively accommodates the volume expansion of S during discharge. TEM images in **Figure 1c** and in our previous work show that HCNTs have hollow structures with a wall thickness of a few nanometers. The hollow part of the HCNT has numerous defects, which can buffer the electrolyte within the tube and facilitate fast charge transfer. The wrinkle-like structure as observed can be seen more clearly in HCNT in **Figure S1**. Correspondingly, the as-prepared HCNTs possess abundant opened edges with geometrical defects. As depicted in **Figures 1d,e**, the 1D/2D HCNT/GO heterostructure is constructed from a self-assembly process rather than from a rough surface. Numerous 1D HCNT and 2D GO are closely entangled. This feature endows the heterostructure with high stability, flexibility, and interconnected porous channels. The heterostructure effectively prevents polysulfide diffusion and accelerates electron transfer for the polysulfide conversion reactions. Thus, the shuttling effect of LSB is remitted. The 3D ferroconcrete-like phenomenon occurs here because of the combination of the special helical structures of HCNTs and O functional groups on the GO surface, which can reinforce their connections. The large rGO not only acts as substrate for the uniform dispersion of the S but also greatly favors the rapid charge transfer in the whole electrode. The HCNTs also improve the electrical conductivity of the material for electron transport. **Figures 1f,g** show that the S particles are well-coated and confined by the GO sheets and HCNT/rGO heterostructures; S is also interfaced with the HCNT sheets. Thus, the fabrication benefited from the synergistic, applicable self-assembly and sulfuration strategy. Therefore, 3D ferroconcrete-like HCNT/rGO/S can reduce dissolution and protect S from decomposition by the electrolyte. The HCNT/rGO heterostructure layer in HCNT/rGO/S, which features a hydrophilic surface, not only prevents polysulfide dissolution but also improves the wettability of the electrolyte with the electrode.

The elemental mapping images in **Figures 1h–j** confirm the uniform distribution of C and S elements within a single HCNT/rGO/S particle. This form reduces dissolution and protects S from electrolyte decomposition. In addition, it can increase the interface contact and surface area, which can enhance the electron transfer pathway. These results indicate that 1D/2D HCNT/rGO heterostructures are successfully constructed. The larger distribution of C points compared with S points confirms that the outer shells of the material consist of C.

XRD is commonly used to study the crystallization of materials. The XRD patterns of HCNT/S, rGO/S, HCNT/rGO/S are shown in **Figure 2**. The three samples show obvious diffraction peaks, and the results indicate that the mixed materials of the samples form a relatively complete crystal structure. HCNT and rGO show a "steamed bread" peak at $2\theta = 20–30°$, indicating that the two C-based materials are present in the sample in an amorphous state (Zhang Y. Z. et al., 2018). The three samples reveal sharp elemental S peaks at $2\theta = 23.187°$, which indicates a typical S_8 bond structure. This characteristic reveals that the material has a remarkable crystal structure in all three samples (Zhang et al., 2014; Xu et al., 2017). The difference is that the sharpness of the S peak decreased in the three samples of HCNT/S, rGO/S, and HCNT/rGO/S. This characteristic indicates that the degree of dispersion and encapsulation of elemental S in the three composite materials increases. The XRD results demonstrate that this structure will exert a very strong inhibitory effect on S diffusion.

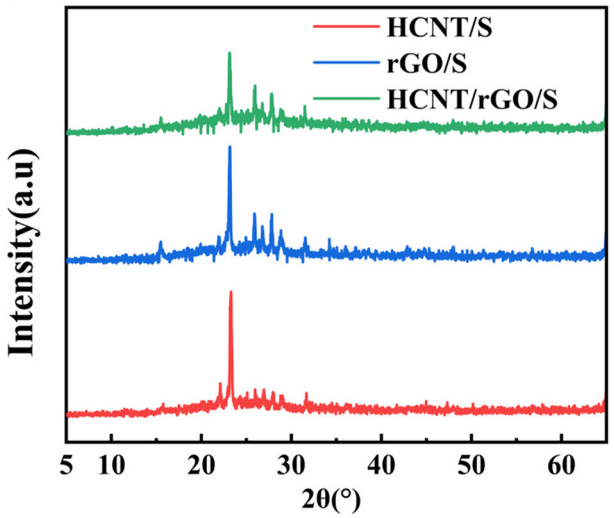

FIGURE 2 | XRD patterns of HCNT/S, reduced graphene oxider GO/S, HCNT/reduced graphene oxider GO/S.

Figure 3 presents the Raman spectra of rGO/S, HCNT/S, and HCNT/rGO/S and further confirm the presence of a graphene matrix in the composites. Two Raman bands were found in the spectra of rGO/S, HCNT/S, and HCNT/rGO/S. The two broad Raman peaks observed at ∼1,351 and 1,599 cm^{-1} could be attributed to the D and G bands of graphite, respectively (Hou et al., 2016). The G-band could be ascribed to sp^2 C vibrations, while the D-band could be ascribed to dispersive, defect-induced vibrations because of the disordered structure of graphene (Ma et al., 2017). I_D/I_G results of *ca.* 1.02, 1.05, and 1.11 are obtained for HCNT/S, rGO/S, and HCNT/rGO/S, respectively. These results reflect the increasing disorder of the 1D/2D heterostructure. The positions of S in the Raman spectrum are located at 153, 218, and 474 cm^{-1} (Zeng et al., 2014). The low intensity of the peaks suggests that the crystalline S clusters are homogeneously dispersed along the HCNT/rGO surface (Yang et al., 2016). After ultrasonic hydrothermal reduction, a facile and green physical coating deposition method is used to wrap S into the HCNT/rGO sheets (HCNT/rGO/S).

XPS measurement was conducted to confirm the incorporation of S into HCNT/rGO (**Figure 4**). **Figure 4A** shows the X-ray photoelectron spectrum of the HCNT/rGO/S composite. The survey spectrum confirms the coexistence of S, C, and O elements in the hybrid paper. The signal of S in the HCNT/rGO/S composite clearly shows the presence of S in the HCNT/rGO matrix. The O signals can be ascribed to residual O

functional groups attached to the surface of rGO. Deconvolution of the C 1s spectrum of the HCNT/rGO/S composite shown in **Figure 4B** reveals three peaks at 286.6, 285.4, and 284.6 eV which can be designated as C–O, C–S, and C–C/C=C species, respectively (Zheng et al., 2017). As illustrated in **Figure 4C**, the binding energy of $2p_{3/2}$ and S $2p_{1/2}$ are 163.8 and 165.1 eV, respectively (Li et al., 2016). The binding energy of 163.8 eV at S $2p_{3/2}$ peak is slightly lower than that of elemental S (164.0 eV), thus suggesting the possible presence of C–S bonds (Wang Z. et al., 2014). In addition, the minor peak at ∼168.6 eV indicates the sulfate species formed by sulfur oxidation in air (Yang et al., 2016).

The weight percentage of S was characterized by thermogravimetric analysis (TGA, **Figure 5**). As shown in **Figure 5**, the weight losses of rGO/S, HCNT/S, and HCNT/rGO/S at 395°C were 87.8, 68.91, and 90.4 wt%. Acid-HCNT and rGO show a weight loss of 0.5 wt% during the process, respectively, indicating that the content of oxhydryl and carboxyl was in acid-HCNT and rGO (Wan et al., 2014). According to the weight loss of HCNT and rGO, the S content in HCNT/rGO/S is 89.5 wt%. The very high S content in HCNT/rGO/S not only allows good loading effects through the porous 3D structure but also maintains sulfur through additional active sites (Liu et al., 2017). Interestingly, the HCNT/rGO/S composite exhibited a higher sublimation temperature, indicating a strong interaction between sulfur and HCNT/rGO (Yang et al., 2018).

Electrochemical Performance

In order to evaluate the electrochemical properties of the composites, the CR-2025 button battery with HCNT/rGO/S as cathode and the Li foil as anode were assembled for testing. On the Neware battery test system, the batteries circulate in the range of 1.5–2.8 V (relative to Li/Li^+), and the specific capacity is calculated based on the S content in the composites.

The Coulomb efficiency of HCNT/rGO/S at 0.1 C and the cycling stability profiles of the three cathodes at various current

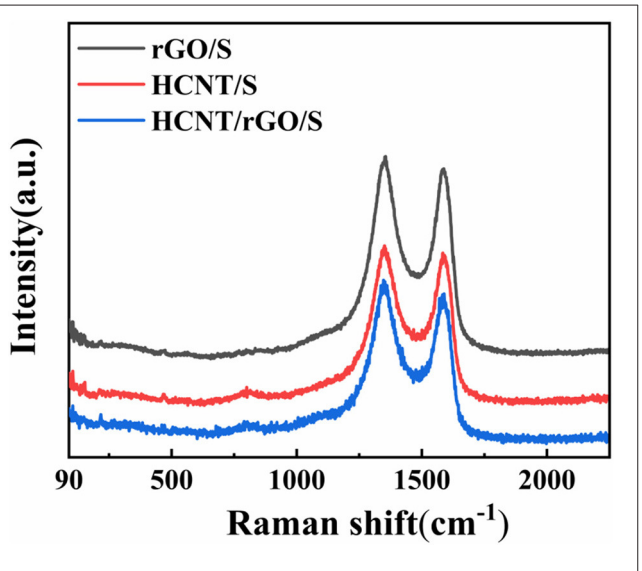

FIGURE 3 | Raman spectra of helical carbon nanotubes (HCNT)/sulfur (S), reduced graphene oxide (rGO)/S, and HCNT/rGO/S.

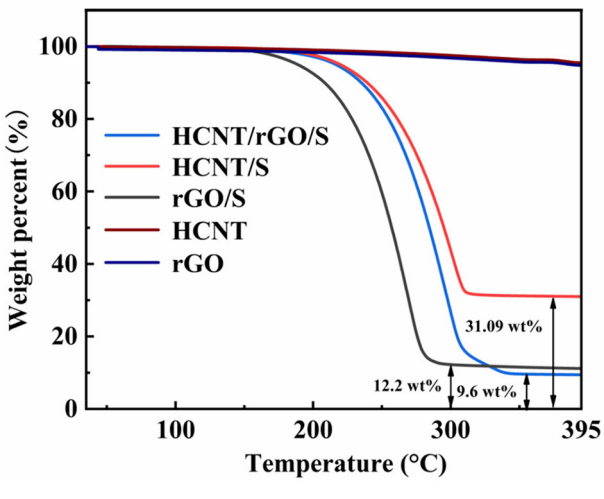

FIGURE 5 | Thermogravimetric (TG) curves for helical carbon nanotubes (HCNT), reduced graphene oxide (rGO), rGO/sulfur (S), HCNT/S, and HCNT/rGO/S from room temperature to 395°C at a heating rate of 10°C min^{-1} under N_2 atmosphere.

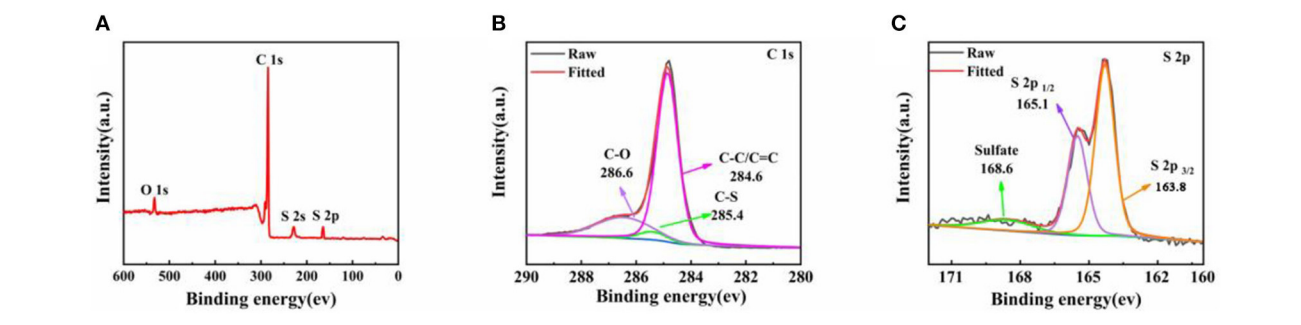

FIGURE 4 | X-ray photoelectron spectroscopy (XPS) survey spectrum of helical carbon nanotubes (HCNT)/reduced graphene oxide (rGO)/sulfur (S) composites **(A)**; C 1s **(B)**, and S 2p **(C)** XPS spectra of the HCNT/rGO/S composite.

densities are shown in **Figure 6**. In **Figure 6A**, the HCNT/rGO/S cathode achieves an initial specific capacity as high as 1,196 mAh g^{-1} at 0.1 C with a high active-S utilization rate of 71.4% and a high initial coulomb efficiency of 96.9%. The cathode retains a high reversible specific capacity of 1,016 mAh g^{-1} after 200 cycles, which corresponds to a capacity retention of 85%. For comparison, HCNT/S and rGO/S cathodes were prepared at the same conditions. The HCNT@S and rGO/S cathodes deliver initial specific discharge capacities of 1,020 and 1,107 mAh g^{-1}, respectively, at 0.1 C and maintain discharge specific capacities of 556 and 723 mAh g^{-1} after 200 cycles, as demonstrated in **Figure 6B**. The HCNT/rGO/S cathode shows superior cycling stability. **Figures 6B–D** show the cycling performance of the HCNT/rGO/S cathode at charge/discharge rates of 0.1, 0.2 and 0.5 C, respectively. After 200 cycles, the HCNT/rGO/S cathode still exhibits a reversible specific capacity of 1,016 mAh g^{-1} at 0.1 C, which corresponds to a capacity retention of 85%. When the current rate increases to 0.2 C, the initial discharge capacity (1,130 mAh g^{-1}) becomes lower than that at 0.1 C, but the cycle stability is significantly improved. A high reversible specific capacity of 971.8 mAh g^{-1} remains after 200 cycles at 0.2 C, which corresponds to a capacity retention of 86%. This behavior is due to the high charge/discharge rate of materials, which weakens the shuttle effect of dissolved polysulfides by decreasing their retention time in the electrolyte in each cycle. Even at a high rate of 0.5 C, the HCNT/rGO/S cathode delivers an initial specific discharge capacity of 1,009 mAh g^{-1}. After 200 cycles, the specific capacity remains at 872 mAh g^{-1}, which translates to a capacity retention of 86.5%. By contrast, the HCNT/S and rGO/S cathodes deliver relatively inferior cycling stabilities of only 490 and 634 mAh g^{-1}, respectively, at 0.5 C after 200 cycles. The superior electrochemical performance (e.g., cycle stability and S utilization ratio) observed in HCNT/rGO/S compared with those of the HCNT/S and rGO/S electrodes could be ascribed to the unique 3D ferroconcrete-like HCNT/rGO architectures. The S particles are well-coated and confined. HCNT prompt the formation of an interconnected 3D network architecture and maintain the structural integrity of the material. The heterostructures and rGO coating, which presents numerous wrinkles, could markedly minimize direct contact between the polysulfide and the electrolyte, thereby improving the nucleation/conversion redox kinetics of the resulting material.

For further comparison, the rate capabilities of HCNT/rGO/S, HCNT/S, and rGO/S cathodes were investigated at various

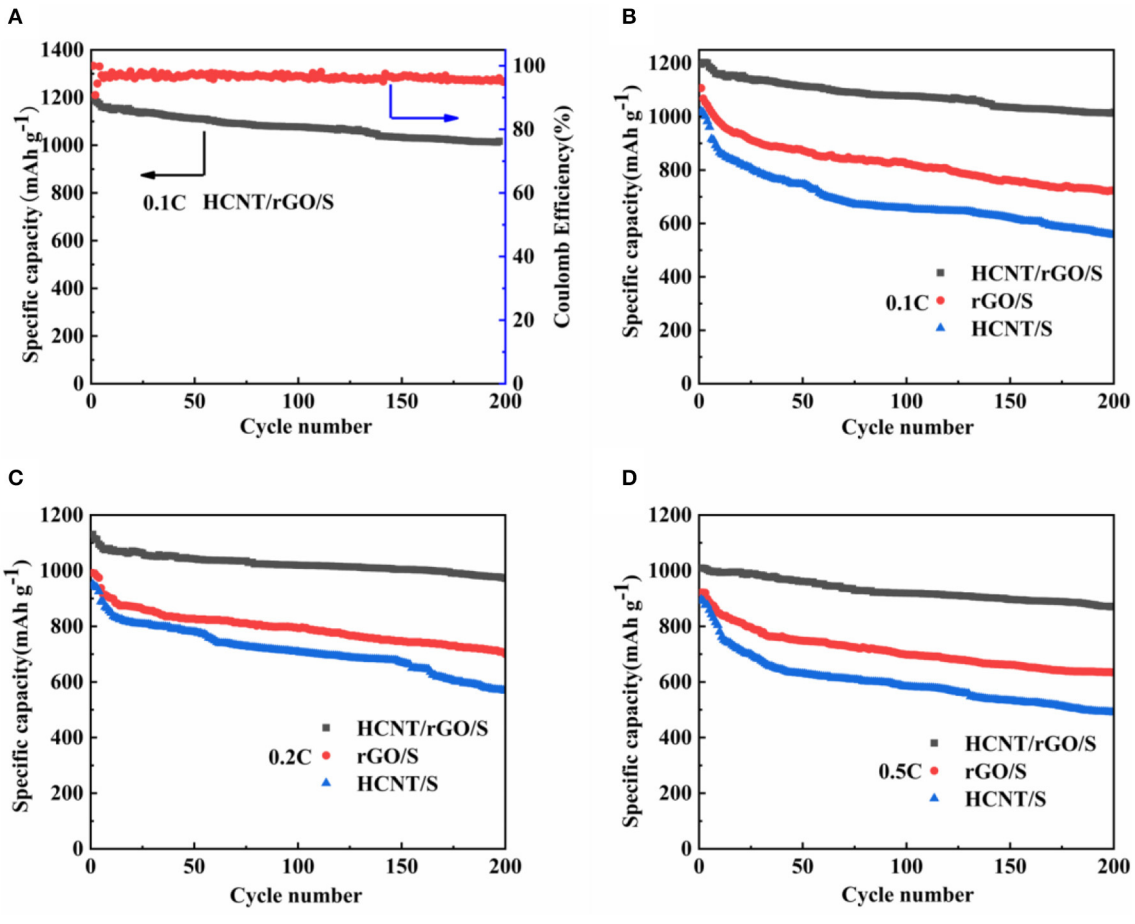

FIGURE 6 | Cycle performance of Li-S cells **(A)** 0.1 C, **(B)** 0.1 C, **(C)** 0.2 C, **(D)** 0.5 C.

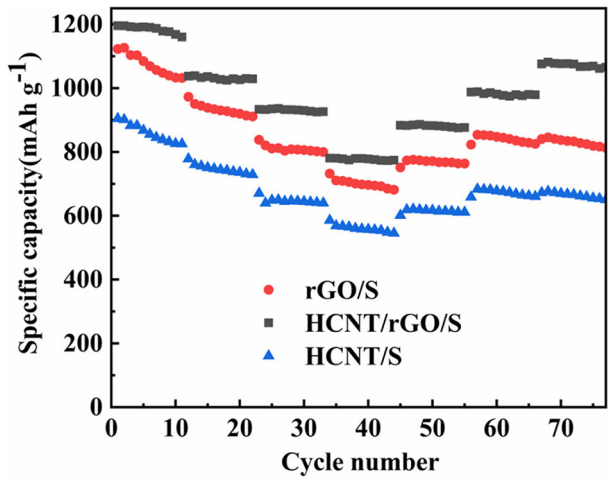

FIGURE 7 | Rate performance of helical carbon nanotubes (HCNT)/sulfur (S), reduced graphene oxide (rGO)/S, HCNT/rGO/S.

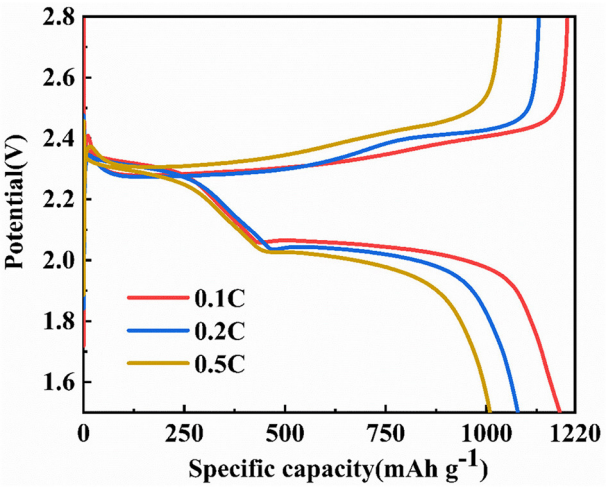

FIGURE 8 | The initial discharge/charge curves of the helical carbon nanotubes (HCNT)/reduced graphene oxide (rGO)/sulfur (S) cathode at various C rates from 0.1 to 0.5 C.

current rates, as depicted in **Figure 7**. The reversible discharge capacities of the cell with the HCNT/rGO/S electrode at 0.1, 0.2, 0.5, and 1 C are 1,195, 1,037, 933, and 780 mAh g^{-1}, respectively. When the current rate is reversed to 0.5, 0.2, and 0.1 C, the HCNT/rGO/S electrode recovers its capacities of 883, 987, and 1,075 mAh g^{-1}, respectively, without abrupt capacity fading. The discharge capacity gradually decreases as the current increases but maintains a considerable discharge capacity. Compared with the HCNT/rGO/S electrode, the rGO/S electrode exhibits relatively low specific capacities and discharge capacities of 1,031, 910, 799, and 681 mAh g^{-1} at the end of the last cycle at rates of 0.1, 0.2, 0.5, and 1 C, respectively. By contrast, the reversible capacities of HCNT/S at current rates of 0.1, 0.2, 0.5, and 1 C are 825, 728, 639, and 545 mAh g^{-1}, respectively. As the current rate increases, the reversible specific capacity decreases. This phenomenon may be attributed to slow electrode kinetics on the electrode/electrolyte interface due to high S loading. The HCNT/rGO/S electrode shows better rate performance than the HCNT/S and rGO/S electrodes because the HCNT of the former are dispersed and wrapped around the GO sheets. The loose and multilevel 3D porosity heterostructure created by the HCNT and rGO helps immobilize S species and maintain the electrical conductivity and excellent polysulfide adsorption capacity of the electrode.

Figure 8 shows the charge and discharge voltage curves of a battery in which HCNT/rGO/S was used as a cathode material. Based on the mass of S in the cathode material, the initial discharge capacities of the cathode at 0.1, 0.2, and 0.5 C are 1,196, 1,130, and 1,009 mAh g^{-1}, respectively, and the initial coulombic efficiency is 96.9% at 0.1 C. **Figure 8** shows that the discharge curves at the different current rates basically have two discharge platforms located at ∼2.3 and 2.0 V, respectively. The platform of ∼2.3 V corresponds to the reduction of S_8 to Li_2S_x ($4 \leq x \leq 8$), and the platform of ∼2.0 V corresponds to the reaction of Li_2S_x ($4 \leq x \leq 8$) to Li_2S_2/Li_2S (Chen et al., 2017). The discharge curves of 0.1 and 0.2 C have a higher discharge platform than the discharge curve at 0.5 C. Moreover, as the current multiplier increases, the length of the discharge platform decreases. With the increase of current rate from 0.1 to 0.5 C, a slight increase in cell polarization (voltage difference between charge platform and second discharge voltage) can be observed in the range of 0.24 to 0.32 V. This phenomenon is mainly due to fact that a large discharge current increases the polarization of the battery, and the larger the discharge current, the more obvious the polarization trend. Even at a high current rate of 0.5 C, the low discharge voltage plateau remained high at 1.95 V, which is higher and further demonstrates the great rate capability (Li et al., 2016; Zheng et al., 2017).

Figure 9A shows a CV curve of a battery prepared with HCNT/rGO/S at a scan rate of 0.1 mV s^{-1} and a voltage range of 1.5–3 V. Two reduction peaks correspond to the formation of higher order Li_2S_x ($4 \leq x \leq 8$) and insoluble Li_2S_2/Li_2S (Yin et al., 2013). The oxidation peak corresponds to the oxidation of the reverse insoluble polysulfide. The small voltage shift between cathodic and anodic peaks reflects the low overvoltage of the cell and indicates the high reversibility of the cell reaction. The HCNT/rGO/S structured cell reveals a large and stable redox peak current density in the CV test. This feature explains the low polarization, good reversibility, and excellent cycle stability.

Figure 9B shows the charge/discharge curves for the 2nd, 10th, 50th, 100th, and 200th cycles of the HCNT/rGO/S battery at 0.1 C. The voltage profiles of the 2nd, 10th, 50th, 100th, and 200th cycles of the HCNT/S and rGO/S cathode at 0.1 C are displayed in **Figure S2**. When tested under the same C rate, two typical Li_2S_x plateaus are observed at 2.25 and 1.9 V for HCNT/S and rGO/S. These values correspond to the formation of high-order and low-order polysulfides, respectively. Greater polarization and the disappearance of the first platform were watched in rGO. This phenomenon could be attributed to the lack of

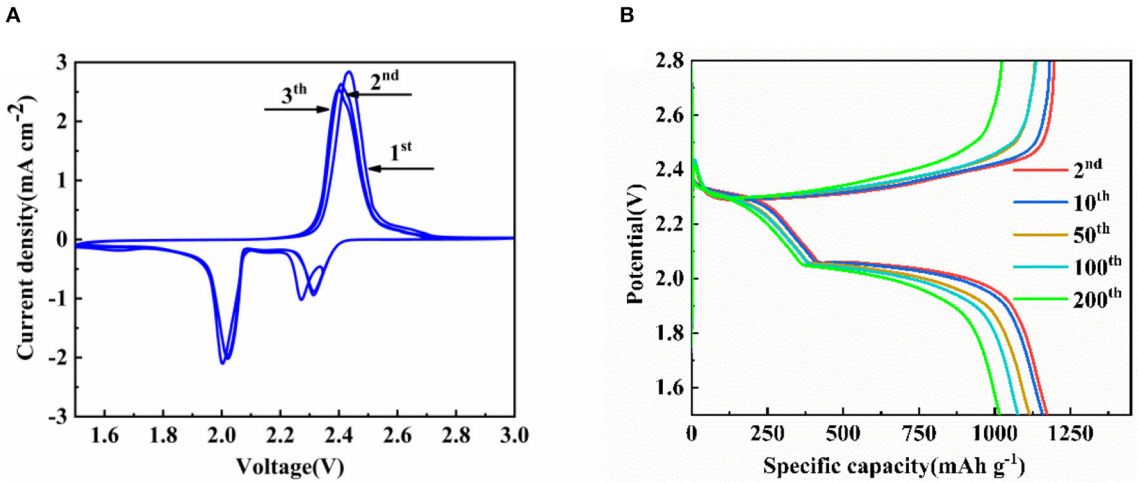

FIGURE 9 | (A) Cyclic voltammetry (CV) curves at the scan rate of 0.1 mV s^{-1} **(B)** from 2nd to 200th discharge/charge curves of helical carbon nanotubes (HCNTs)/reduced graphene oxide (rGO)/sulfur (S) cathode at 0.1 C between 1.5 and 2.8 V.

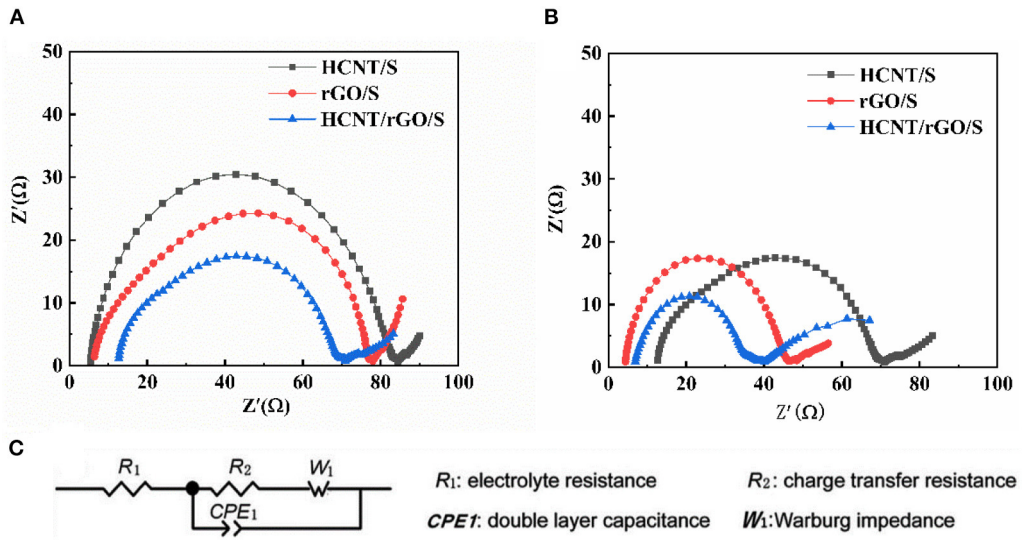

FIGURE 10 | Electrochemical impedance spectrum (EIS) of the cells with different cathodes **(A)** before cycling and **(B)** after cycling at 0.1 C.

conductivity of the material, which results in a markedly lower capacity compared with that of thermally reduced or HCNT-containing materials. In **Figure 9B**, the 2.3 V upper discharge platform of the HCNT/rGO/S indicates that the reduction of S leads to the formation of soluble polysulfides. Rapid S (solid)–polysulfide (liquid) reduction involves the formation, dissolution, and diffusion of polysulfides. The hysteresis between charging and discharging increases slightly as the number of cycles increases.

To investigate the effect of HCNTs on the electrochemical performance of the cell, we performed EIS after rate performance and constant-current charge/discharge testing (**Figure 10**). Impedance testing was performed in an electrochemical workstation over the frequency range of 0.01–100 kHz. In the fitted graph, R_1 represents the electrolyte resistance, R_2 represents the charge transfer resistance, W_1 represents the Walburg diffusion resistance, and CPE_1 is a constant phase. The three Nyquist diagrams of HCNT/S, rGO/S, and HCNT/rGO/S are composed of a semicircle at high intermediate frequencies, primarily because of interactions between electrolyte resistance and charge transfer resistance (Liang et al., 2016). The oblique line at low frequencies is closely related to the diffusion process of Li^+. The ohmic resistance is shown by the intercept of the high frequency semicircle on the coordinate axis (He et al., 2016). Comparison of the diameters of the semicircles in **Figures 10A,B** shows that the charge transfer resistance of the three samples of HCNT/S, rGO/S, and HCNT/rGO/S sequentially decreases. This result indicates that the 3D structural material has extremely excellent electrical conductivity. Comparison of the same materials shows that the charge transfer resistance after cycling

is smaller than that before cycling and that the redistribution process of the active material reduces the electric resistance (Ummethala et al., 2018). Thus, the active material has a considerable utilization rate for recharging and discharging.

CONCLUSION

In summary, we achieved the facile fabrication of a 3D HCNT/rGO/S composite bearing a ferroconcrete-like network. The unique interconnected S–HCNTs framework effectively improves electron conductivity, prevents polysulfide dissolution and minimizes the shuttle effect in the composite. Combination of HCNTs and rGO coatings reinforces electrode stability and provides pathways for rapid electron transport; the 3D structure provides effective ion diffusion channels. The rGO outer layers and heterostructures formed with HCNT confine S species and enhance the hydrophilicity of the electrolyte. These synergistic advantages endow the HCNT/rGO/S electrode with an initial discharge capacity of 1,196 mAh g^{-1} and stable reversible capacity of 1,016 mAh g^{-1} after 200 cycles at 0.1 C. The remarkable improvement of the electrochemical performance of the electrode indicates the importance of rationally designing the 3D structure and chemical interaction of S composite materials for Li-S batteries and other energy storage fields, such as Li-air batteries, Na-ion batteries, and supercapacitors.

DATA AVAILABILITY STATEMENT

All datasets generated for this study are included in the article/**Supplementary Material**.

AUTHOR CONTRIBUTIONS

All authors listed have made a substantial, direct and intellectual contribution to the work, and approved it for publication.

FUNDING

This work was financially supported by National Natural Science Foundation of China (51662004, 11604061, 11664007, and 11764011), Natural Science Foundation of Guangxi Zhuang Autonomous Region of China (2018GXNSFAA281191 and 2018GXNSFAA050014). Supported by Foundation of Guilin University of Technology (GLUTQD2002023).

SUPPLEMENTARY MATERIAL

The Supplementary Material for this article can be found online at: https://www.frontiersin.org/articles/10.3389/fenrg.2019.00157/full#supplementary-material

REFERENCES

Akagi, K., Tamura, R., Tsukada, M., Itoh, S., and Ihara, S. (1995). Electronic structure of helically coiled cage of graphitic carbon. *Phys Rev Lett*. 74, 2307–2310. doi: 10.1103/PhysRevLett.74.2307

Chen, T., Cheng, B., Zhu, G., Chen, R., Hu, Y., Ma, L., et al. (2017). Highly efficient retention of polysulfides in "sea urchin"-like carbon nanotube/nanopolyhedra superstructures as cathode material for ultralong-life lithium-sulfur batteries. *Nano Lett.* 17, 437–444. doi: 10.1021/acs.nanolett.6b04433

Cherusseri, J., Sharma, R., and Kar, K. K. (2016). Helically coiled carbon nanotube electrodes for flexible supercapacitors. *Carbon N. Y.* 105, 113–125. doi: 10.1016/j.carbon.2016.04.019

Di, J., Fang, S., Moura, F. A., Galvao, D. S., Bykova, J., Aliev, A., et al. (2016). Strong, twist-stable carbon nanotube yarns and muscles by tension annealing at extreme temperatures. *Adv. Mater*. 28, 6598–6605. doi: 10.1002/adma.201600628

Ding, Y.-L., Kopold, P., Hahn, K., van Aken, P. A., Maier, J., and Yu, Y. (2016). Facile solid-state growth of 3D well-interconnected nitrogen-rich carbon nanotube-graphene hybrid architectures for lithium-sulfur batteries. *Adv. Funct. Mater*. 26, 1112–1119. doi: 10.1002/adfm.201504294

Gu, S., Sun, C., Xu, D., Lu, Y., and Wen, Z. (2018). Recent progress in liquid electrolyte-based li–s batteries: shuttle problem and solutions. *Electrochem. Energ. Rev*. 1:599. doi: 10.1007/s41918-018-0021-0

Gulzar, U., Li, T., Bai, X., Colombo, M., Ansaldo, A., Marras, S., et al. (2018). Nitrogen-doped single-walled carbon nanohorns as a cost-effective carbon host toward high-performance lithium-sulfur batteries. *ACS Appl. Mater. Interfaces* 10, 5551–5559. doi: 10.1021/acsami.7b17602

He, J., Chen, Y., Lv, W., Wen, K., Xu, C., Zhang, W., et al. (2016). Three-dimensional CNT/graphene–Li_2S aerogel as freestanding cathode for high-performance Li–S batteries. *ACS Energy Lett*. 1, 820–826. doi: 10.1021/acsenergylett.6b00272

Hou, Y., Li, J., Gao, X., Wen, Z., Yuan, C., and Chen, J. (2016). 3D dual-confined sulfur encapsulated in porous carbon nanosheets and wrapped with graphene aerogels as a cathode for advanced lithium sulfur batteries. *Nanoscale* 8, 8228–8235. doi: 10.1039/C5NR09037G

Hu, G., Sun, Z., Shi, C., Fang, R., Chen, J., Hou, P., et al. (2017). A sulfur-rich copolymer@CNT hybrid cathode with dual-confinement of polysulfides for high-performance lithium-sulfur batteries. *Adv. Mater.* 29:1603835. doi: 10.1002/adma.201603835

Jin, F., Xiao, S., Lu, L., and Wang, Y. (2016). Efficient activation of high-loading sulfur by small CNTs confined inside a large CNT for high-capacity and high-rate lithium-sulfur batteries. *Nano Lett.* 16, 440–447. doi: 10.1021/acs.nanolett.5b04105

Kim, J., Lee, D.-J., Jung, H.-G., Sun, Y.-K., Hassoun, J., and Scrosati, B. (2013). An advanced lithium-sulfur battery. *Adv. Funct. Mater*. 23, 1076–1080. doi: 10.1002/adfm.201200689

Kim, K. H., Oh, Y., and Islam, M. F. (2012). Graphene coating makes carbon nanotube aerogels superelastic and resistant to fatigue. *Nat. Nanotechnol.* 7, 562–566. doi: 10.1038/nnano.2012.118

Li, G., Sun, J., Hou, W., Jiang, S., Huang, Y., and Geng, J. (2016). Three-dimensional porous carbon composites containing high sulfur nanoparticle content for high-performance lithium-sulfur batteries. *Nat. Commun.* 7:10601. doi: 10.1038/ncomms10601

Li, X., Xu, Y., Hu, G., Luo, Z., Xu, D., Tang, T., et al. (2018). Self-assembled formation of conjugated 3D reduced graphene oxide-wrapped helical CNTs nanostructure and nitrogen-doped using photochemical doping for high-performance supercapacitor electrodes. *Electrochim. Acta* 280, 33–40. doi: 10.1016/j.electacta.2018.05.106

Liang, G., Wu, J., Qin, X., Liu, M., Li, Q., He, Y., et al. (2016). Ultrafine TiO_2 decorated carbon nanofibers as multifunctional interlayer for high-performance lithium–sulfur battery. *ACS Appl. Mater. Interfaces* 8, 23105–23113. doi: 10.1021/acsami.6b07487

Liu, M., Qin, X., He, Y., Li, B., and Kang, F. (2017). Recent innovative configurations in high-energy lithium–sulfur batteries. *J. Mater. Chem. A* 5:5222–5234. doi: 10.1039/C7TA00290D

Ma, Z., Tao, L., Liu, D., Li, Z., Zhang, Y., Liu, Z., et al. (2017). Ultrafine nano-sulfur particles anchored on *in situ* exfoliated graphene for lithium–sulfur batteries. *J. Mater. Chem. A* 5, 9412–9417. doi: 10.1039/C7TA01981E

Manthiram, A., Fu, Y., and Su, Y. S. (2013). Challenges and prospects of lithium-sulfur batteries. *Acc. Chem. Res.* 46, 1125–1134. doi: 10.1021/ar300179v

Peng, H.-J., Huang, J.-Q., Zhao, M.-Q., Zhang, Q., Cheng, X.-B., Liu, X.-Y., et al. (2014). Nanoarchitectured graphene/CNT@porous carbon with extraordinary electrical conductivity and interconnected micro/mesopores for lithium-sulfur batteries. *Adv. Funct. Mater.* 24, 2772–2781. doi: 10.1002/adfm.201303296

Song, M. K., Cairns, E. J., and Zhang, Y. (2013). Lithium/sulfur batteries with high specific energy: old challenges and new opportunities. *Nanoscale* 5, 2186–2204. doi: 10.1039/c2nr33044j

Su, D., Cortie, M., and Wang, G. (2017). Fabrication of N-doped graphene-carbon nanotube hybrids from prussian blue for lithium-sulfur batteries. *Adv. Energy Mater.* 7:1602014. doi: 10.1002/aenm.201602014

Sun, C. L., Chang, C. T., Lee, H. H., Zhou, J., Wang, J., Sham, T. K., et al. (2011). Microwave-assisted synthesis of a core-shell MWCNT/GONR heterostructure for the electrochemical detection of ascorbic acid, dopamine, and uric acid. *ACS Nano* 5, 7788–7795. doi: 10.1021/nn2015908

Tan, L., Li, X., Wang, Z., Guo, H., and Wang, J. (2018). Lightweight reduced graphene oxide@MoS_2 interlayer as polysulfide barrier for high-performance lithium-sulfur batteries. *ACS Appl. Mater. Interfaces* 10, 3707–3713. doi: 10.1021/acsami.7b18645

Tang, N., Wen, J., Zhang, Y., Liu, F., Lin, K., and Du, Y. (2010). Helical carbon nanotubes: catalytic particle size-dependent growth and magnetic properties. *ACS Nano* 4, 241–250. doi: 10.1021/nn901425r

Ummethala, R., Fritzsche, M., Jaumann, T., Balach, J., Oswald, S., Nowak, R., et al. (2018). Lightweight, free-standing 3D interconnected carbon nanotube foam as a flexible sulfur host for high performance lithium-sulfur battery cathodes. *Energy Storage Mater.* 10, 206–215. doi: 10.1016/j.ensm.2017.04.004

Wan, C., Wu, W., Wu, C., Xu, J., and Guan, L. (2014). A layered porous ZrO2/RGO composite as sulfur host for lithium–sulfur batteries. *RSC Adv.* 5, 5102–5106. doi: 10.1039/C4RA12031K

Wang, B., Hu, C., and Dai, L. (2016). Functionalized carbon nanotubes and graphene-based materials for energy storage. *Chem. Commun.* 52, 14350–14360. doi: 10.1039/C6CC05581H

Wang, C., Su, K., Wan, W., Guo, H., Zhou, H., Chen, J., et al. (2014). High sulfur loading composite wrapped by 3D nitrogen-doped graphene as a cathode material for lithium–sulfur batteries. *J. Mater. Chem. A* 2, 5018–5023. doi: 10.1039/C3TA14921H

Wang, L., Liu, J., Haller, S., Wang, Y., and Xia, Y. (2015). A scalable hybrid separator for a high performance lithium-sulfur battery. *Chem. Commun.* 51, 6996–6999. doi: 10.1039/C5CC00444F

Wang, Z., Dong, Y., Li, H., Zhao, Z., Wu, H. B., Hao, C., et al. (2014). Enhancing lithium-sulphur battery performance by strongly binding the discharge products on amino-functionalized reduced graphene oxide. *Nat. Commun.* 5:5002. doi: 10.1038/ncomms6002

Xiaofei, Y., Xia, L., Keegan, A., Huamin, Z., and Xueliang, S. (2018). Structural design of lithium–sulfur batteries: from fundamental research to practical application. *Electrochem. Energ. Rev.* 1, 239–293. doi: 10.1007/s41918-018-0010-3

Xu, Y., Li, X., Hu, G., Wu, T., Luo, Y., Sun, L., et al. (2017). Graphene oxide quantum dot-derived nitrogen-enriched hybrid graphene nanosheets by simple photochemical doping for high-performance supercapacitors. *Appl. Surf. Sci.* 422, 847–855. doi: 10.1016/j.apsusc.2017.05.189

Yan, Y., Yin, Y.-X., Xin, S., Su, J., Guo, Y.-G., and Wan, L.-J. (2013). High-safety lithium-sulfur battery with prelithiated Si/C anode and ionic liquid electrolyte. *Electrochim. Acta* 91, 58–61. doi: 10.1016/j.electacta.2012.12.077

Yang, W., Yang, W., Song, A., Sun, G., and Shao, G. (2018). 3D interconnected porous carbon nanosheets/carbon nanotubes as a polysulfide reservoir for high performance lithium-sulfur batteries. *Nanoscale* 10, 816–824. doi: 10.1039/C7NR06805K

Yang, X., Zhu, W., Cao, G., and Zhao, X. (2016). Preparation of a carbon nanofibers–carbon matrix–sulfur composite as the cathode material of lithium–sulfur batteries. *RSC Adv.* 6, 7159–7171. doi: 10.1039/C5RA24129D

Yin, Y. X., Xin, S., Guo, Y. G., and Wan, L. J. (2013). Lithium-sulfur batteries: electrochemistry, materials, and prospects. *Angew. Chem. Int. Ed. Engl.* 52, 13186–13200. doi: 10.1002/anie.201304762

Yu, D., Goh, K., Wang, H., Wei, L., Jiang, W., Zhang, Q., et al. (2014). Scalable synthesis of hierarchically structured carbon nanotube-graphene fibres for capacitive energy storage. *Nat. Nanotechnol.* 9, 555–562. doi: 10.1038/nnano.2014.93

Zeng, Q., Wang, D.-W., Wu, K.-H., Li, Y., Condi de Godoi, F., and Gentle, I. R. (2014). Synergy of nanoconfinement and surface oxygen in recrystallization of sulfur melt in carbon nanocapsules and the related Li–S cathode properties. *J. Mater. Chem. A* 2:6439. doi: 10.1039/c4ta00314d

Zhang, H., Liao, X., Guan, Y., Xiang, Y., Li, M., Zhang, W., et al. (2018). Lithiophilic-lithiophobic gradient interfacial layer for a highly stable lithium metal anode. *Nat. Commun.* 9:3729. doi: 10.1038/s41467-018-06126-z

Zhang, H., Zhao, Z., Hou, Y.-N., Tang, Y., Liang, J., Liu, X., et al. (2019). Highly stable lithium–sulfur batteries based on p–n heterojunctions embedded on hollow sheath carbon propelling polysulfides conversion. *J. Mater. Chem. A* 7, 9230–9240. doi: 10.1039/C9TA00975B

Zhang, Y. Z., Liu, S., Li, G. C., Li, G. R., and Gao, X. P. (2014). Sulfur/polyacrylonitrile/carbon multi-composites as cathode materials for lithium/sulfur battery in the concentrated electrolyte. *J. Mater. Chem. A* 2, 4652–4659. doi: 10.1039/C3TA14914E

Zhang, Y. Z., Zhang, Z., Liu, S., Li, G. R., and Gao, X. P. (2018). Free-standing porous carbon nanofiber/carbon nanotube film as sulfur immobilizer with high areal capacity for lithium-sulfur battery. *ACS Appl. Mater. Interfaces* 10, 8749–8757. doi: 10.1021/acsami.8b00190

Zheng, C., Niu, S., Lv, W., Zhou, G., Li, J., Fan, S., et al. (2017). Propelling polysulfides transformation for high-rate and long-life lithium–sulfur batteries. *Nano Energy* 33, 306–312. doi: 10.1016/j.nanoen.2017.01.040

Conflict of Interest: The authors declare that the research was conducted in the absence of any commercial or financial relationships that could be construed as a potential conflict of interest.